International Journal of Solids and Structures 46 (2009) 1436–1447

Contents lists available at ScienceDirect

International Journal of Solids and Structures

journal homepage: www.elsevier.com/locate/ijsolstr

Conical indentation of incompressible rubber-like materials

A.E. Giannakopoulos, D.I. Panagiotopoulos *

Laboratory for Strength of Materials and Micromechanics, Department of Civil Engineering, University of Thessaly, Volos 38336, Greece

ARTICLE INFO

Article history:
Received 5 July 2008
Received in revised form 3 November 2008
Available online 18 November 2008

Keywords:
Rubber materials
Incompressibility
Conical indentation
Hyperelasticity
Finite elements

ABSTRACT

In the last decade, the indentation test has become a useful tool for probing mechanical properties of small material volumes. In this context, little has been done for rubber-like materials (elastomers), although there is pressing need to use instrumented indentation in biomechanics and tissue examination. The present work investigates the quasi-static normal instrumented indentation of incompressible rubber-like substrates by sharp rigid cones. A second-order elasticity analysis was performed in addition to finite element analysis and showed that the elastic modulus at infinitesimal strains correlates well with the indentation response that is the relation between the applied force and the resulting vertical displacement of the indentor's tip. Three hyperelastic models were analyzed: the classic Mooney–Rivlin model, the simple Gent model and the one-term Ogden model. The effect of the angle of the cone was investigated, as well as the influence of surface friction. For blunt cones, the indentation response agrees remarkably well with the prediction of linear elasticity and confirms available experimental results of instrumented Vickers indentation.

1. Introduction

The response of material substrates to indentation by rigid indentors in the form of spheres, cones and pyramids is referred to as "hardness" testing. "Hardness" has been classically referred to the indentation of metal substrates and implies a permanent dent on the surface of the substrate upon unloading. This cannot be observed on rubber-like surfaces at ambient temperatures, because of the complete rebound of the surface as soon as the indentor is withdrawn. Currently, hardness testing of elastomers is based on the, so called, Shore test (after A.F. Shore who suggested the test in 1907, Lysaght and DeBellis, 1969) that uses the durometer (a measuring device of a hardened indentor with an accurately calibrated spring, a depth indicator and a flat presser foot). The "Shore hardness" is a number between 0 and 100, which has no obvious correlation with any fundamental mechanical property of the material (e.g. elastic modulus, uniaxial stress–strain response, etc.) and is defined by various standards, e.g. ASTM D 2240, BS 903, ISO 7619, etc. (ASTM, 2003; BS 903, 1997; ISO 7619-I and II, 2004). Elastomers have a Shore hardness number between 30 and 90. The development and standardizing hardness test methods and instruments for rubber materials over the years are in the books of Soden (1951) and Brown (2006). Indentation "hardness" has been known in rubber technology to be a measure of the elastic modulus (Davey and Payne, 1964; Eirich, 1978; Gent, 1992).

The mechanical behavior of elastomers involves large geometric changes of their initial shapes and strong non-linearity between the stresses and strains that develop upon loading. Such mechanical behavior is modeled adequately by hyperelasticity (Green and Adkins, 1970; Ogden, 1984; Antman, 1995). In the context of hyperelasticity, the stress–strain relations are deduced from a single function, W, which describes the elastic strain energy density in the undeformed configuration and is represented by a variety of models which conform with uniaxial tension experiments up to a certain level of straining. At this point, it is worth mentioning that hyperelasticity models serve well in the description of certain biomaterials, including soft tissues, cells and the DNA (Fung, 1993, 1994). This is not very surprising, since the biological molecules are mainly long chains of covalently bonded carbon and hydrogen atoms can be modeled by entropic elasticity (Treloar, 1975). Pathological soft tissues show different elastic behavior, as compared to healthy tissues. For example, the cancerous tissue is 3–7 times stiffer than the normal tissue (Krouskop et al., 1998). Diabetes can increase the stiffness of the soft tissues of feet, causing pain in the region of the heel (Zheng et al., 2000).

An extension of the classic hardness test is the instrumented indentation test, where the applied force on the indentor, P, is recorded simultaneously with the vertical displacement, D, of the indentor's tip into the substrate of the material to be tested. There are clear advantages of the indentation tests in probing mechanical properties of very small volumes of materials and during the last decade there have been strong advancements on the measuring devices performing micro and nano-indentation (Fisher-Cripps, 2002). To interpret the P–D response, there

* Corresponding author. Tel.: +306937293389.
E-mail address: dimpanagiot@yahoo.com (D.I. Panagiotopoulos).

0020-7683/$ - see front matter © 2008 Elsevier Ltd. All rights reserved.
doi:10.1016/j.ijsolstr.2008.11.008

must be a robust and meaningful contact analysis, which can provide relations of the *P–D* response with the mechanical properties. Such relations do not exist so far for cone indentation of rubber materials; the problem is not easy because rubbers do not obey simple constitutive laws. Experiments presenting results of instrumented cone indentations of rubber substrates can be found in rather few references (Sabey, 1958; Greenwood and Tabor, 1958; Crawford and Stephens, 1985; Briscoe et al., 1994; Vallet and Barquins, 2002; Lim and Chaudhri, 2004). The problem is difficult and there are few analytical solutions, even for the non-linear Boussinesq problem (a compressive point force normal to the surface) (Simmonds and Warne, 1994; Gao, 2001; Lee et al., 2004).

To the best of our knowledge, there has been no systematic finite element analysis of the cone indentation of rubber materials. There have been, however, a few papers dealing with finite element analysis of spherical and flat punch of rubber materials. It is important to state briefly the basic findings of these papers, keeping in mind that there can be many pitfalls that accompany these calculations, as discussed by Jabareen and Rubin (2007). They have examined the response of commercially available codes and have detected possible hourglass buckling modes of deformation, especially if little care is taken for the incompressibility constraint. Chang and Sun (1991) investigated the spherical indentation of a simple Ogden material. They found good correlation with the Hertzian solution and a very small effect of the friction at the interface (friction coefficient up to 1). Busfield and Thomas (1999) also examined the spherical indentation of a power law Neo-Hookean material. They investigated the effect of finite thickness and of friction. They found that friction renders a stiffer indentation response for very soft materials and for large penetration depths. Gent and Yeoh (2006) investigated a flat circular punch on a nearly incompressible Neo-Hookean material. They found that the way the outer boundaries are constrained influences the indentation response. Constrained vertical sides away from the contact area produce stiffer response than that predicted by linear elasticity. They also examined the effect of pre-compression of the substrate.

In order to solve the problem of indentation of a rubber substance by a rigid cone, we used a non-linear analysis of second order and derived closed form results that connect the indentation depth D, the contact radius α, the half-angle of the cone $\pi/2-\varphi$ and the applied vertical load P. We confirmed and extended the analytic results with finite element analysis using three well-known constitutive models (Mooney–Rivlin, simple Gent and one-term Ogden). We also examined the influence of Coulomb friction. To the best of our knowledge such analysis has never been undertaken in the past. The results of our analytical efforts were compared with available instrumented indentation tests with steel conical indentors of different angle. The paper concludes with direct comparison of the different models. Finally, we discuss the findings and propose an inverse methodology to predict mechanical properties of rubber materials from conical instrumented indentation tests.

2. Approximate analysis

The equations of equilibrium and the boundary conditions for an elastic body in the absence of body and inertia force, neglecting terms of higher degree than the second of the space derivative of the displacements u_i can be formulated according to Rivlin (1953). The starting point is an elastic strain density energy function W in the reference configuration, of the form suggested by Murnaghan (1951)

$$W=\alpha_1 J_2+\alpha_2 J_1^2+\alpha_3 J_1 J_2+\alpha_4 J_1^3+\alpha_5 J_3, \tag{1}$$

where $\alpha_1,\alpha_2,\alpha_3,\alpha_4,\alpha_5$ are constants and J_1, J_2, J_3 are invariants of the Lagrange strain tensor $\gamma_{ij}=\frac{1}{2}\left(\frac{\partial u_i}{\partial x_j}+\frac{\partial u_j}{\partial x_i}+\frac{\partial u_k}{\partial x_i}\frac{\partial u_k}{\partial x_j}\right)$, where x_i are the Cartesian coordinates of a material point in the undeformed configuration. The function W describes a compressible material. When expressed in terms of principal stretches $\lambda_1,\lambda_2,\lambda_3$, the invariants are

$$J_1=I_1-3,\quad J_2=I_2-2I_1+3,$$
$$J_3=I_3-I_2+I_1-1=(I_3-1)-(J_1+J_2). \tag{2}$$

And

$$I_1=\lambda_1^2+\lambda_2^2+\lambda_3^2,\quad I_2=\lambda_1^2\lambda_2^2+\lambda_2^2\lambda_3^2+\lambda_1^2\lambda_3^2,\quad I_3=\lambda_1^2\lambda_2^2\lambda_3^2 \tag{3}$$

Note that the constants α_1 and α_2 are related with the Lame constants λ, μ of the linear elasticity, at small deformations ($\lambda_i\to 1$)

$$\lambda=4(\alpha_1+2\alpha_2),\quad \mu=-2\alpha_1 \tag{4}$$

with $\alpha_1<0$, $\alpha_2>0$ and $\alpha_1+4\alpha_2>0$.

As we will show later, there is a question as to how the limit of a compressible analysis will describe adequately the incompressible rubber. We let the total displacements be decomposed as

$$u_i=\upsilon_i+w_i, \tag{5}$$

where υ_i and w_i are the first and the second-order displacements, respectively.

2.1. Contact problem of a rigid cone indentor

We consider the contact problem of a rigid indentor whose axis of symmetry is normal to the contact plane. We choose cylindrical polar coordinates (r,θ,z) such that the contact plane is $z=0$ (Fig. 1). In this section, the polar coordinates are taken as material coordinates (undeformed configuration). Although adhesion can be important at low indentation loads and friction may be important at certain cone angles, we will ignore both for the sake of simplicity in this analysis. Friction will be discussed later when full finite element analysis will be presented.

We consider the case of the half space $z\geqslant 0$ deformed by the normal penetration of a rigid cone of angle $2(\pi/2-\varphi)$ as shown in Fig. 1. For this problem, we take $\varepsilon=\tan\varphi$,

$$f(r)=r\tan\varphi=\varepsilon r. \tag{6}$$

For convergence, $\varepsilon=\tan\phi\ll 1\Rightarrow\phi\ll\pi/4$.

The total load P required to produce penetration $D-f(r)$ for $r<\alpha$ is given by integrating the nominal tractions at the contact region, $t_{zz}(r,0)$,

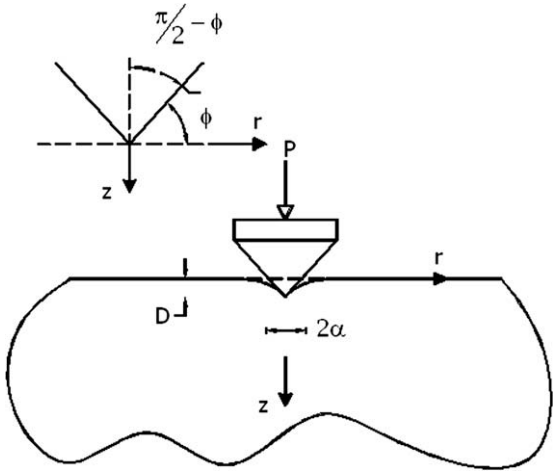

Fig. 1. Schematic of the conical indentation problem.

$$P = -2\pi \int_0^{\alpha} r t_{zz}(r,0)\mathrm{d}r. \tag{7}$$

The displacements and the stress field for the linear problem are given by Johnson (1985) and Sneddon (1972) and depend on

$$\mu = -2\alpha_1, \quad n = \frac{a_1 + 2a_2}{a_1 + 4a_2}, \tag{8}$$

which are the shear modulus and the Poisson ratio, respectively, at zero straining.

Note that, at the tip of the cone, the first-order stresses that depend on the Poisson ratio, Eq. (8), show a logarithmic singularity. This will create problems in the second linear problem. However, the region of the singularity is small and, as Choi and Shield (1981) suggested, it may not be a major problem for obtaining the overall force-depth-contact relations. On the other hand, Picu (1996) investigated the elastic stress singularity of the axisymmetric problem at the vertex of a conical sector attached to a conical notch, where the shear stress is zero at the interface. He found a power type of stress singularity that becomes more intense as the angle of the cone becomes sharper. A power type of stress was also found by Gao and Mai (2002), however, their analysis implies singular stretches at the surface. We will show later the nature of the singularity at the cone tip, as predicted by detailed finite elements. At the moment, it is sufficient to accept this singularity for blunt cones.

In the original formulation of the second-order analysis (Rivlin, 1953; Sabin and Kaloni, 1983), the limiting case of incompressible material was to take $n \to 0.5$ and the constants to take the limiting forms

$$\alpha_1 = -\frac{\mu}{2}, \quad \alpha_2 = \frac{\mu(1-n)}{4(1-2n)}, \quad \alpha_3 = \frac{\mu(5-6n)}{8(1-2n)}, \quad \alpha_4 = \frac{-3\mu(1-n)}{16(1-2n)}, \quad \alpha_5 = \frac{-3\mu}{4}. \tag{9}$$

A problem, however, appears using the above limit. The normal traction at the surface predicts a $1/r$ singularity at the contact center. This means that close to the tip of the cone, contact with the surface will be lost, suggesting the presence of an expanding region, as Gao (2001) predicted for the case of a concentrated load. Unless we assume the presence of a liquid that can fill the gap between the tip and the surface, the above limit is not valid, see also Lee et al. (2004). It is clear that the problem stems from the way that the incompressible limit was taken, resulting to second-order body forces.

Selecting the constants as

$$\alpha_1 = -\frac{\mu}{2}, \quad \alpha_2 = 0, \quad \alpha_3 = 0, \quad \alpha_4 = 0, \quad \alpha_5 = \frac{-3\mu}{4}, \tag{10}$$

the strain energy density approaches the Mooney–Rivlin incompressible model with equal constants

$$W = c_1 J_2 + 3c_1 J_1 = c_1(I_1 - 3) + c_1(I_2 - 3). \tag{11}$$

In this case, $\mu = 4c_1$ is the shear modulus at zero straining. Shield (1967) proved that the energy density described by (11) leads to second-order problem without the influence of the artificial body forces, see also Choi and Shield (1981). Using the limits (10), we obtain

$$t_{zz}(r,0) = -2\mu\varepsilon \ln\left[\left(\alpha + \sqrt{\alpha^2 - r^2}\right)/r\right], \quad 0 \leqslant r \leqslant \alpha, \tag{12}$$

$$D = D_1 = \alpha\varepsilon\frac{\pi}{2} = \alpha\frac{\pi}{2}\tan\phi \Rightarrow \alpha_0 = \frac{2D}{\pi\tan\phi}, \tag{13}$$

$$P = 2\pi\mu\alpha^2\varepsilon = \frac{8\mu D^2}{\pi\tan\phi} = \frac{8ED^2}{3\pi\tan\phi} = C_0 D^2, \tag{14}$$

where $E = 3\mu$ is the elastic modulus at infinitesimal strains. This solution retains the logarithmic singularity of the stresses at the cone tip. As will be shown later, for blunt cones, the finite element results indicate that this is a reasonable approximation. The macroscopic response summarized by Eqs. (13) and (14) suggests that the linear elasticity results hold true for blunt cone indentors and substrates that follow the particular Mooney–Rivlin response, as of Eq. (11). These unexpected results were confirmed for blunt cones by finite elements, as will be shown below.

2.2. Second-order incompressible elasticity

The previous results indicate the need for a second-order incompressible elasticity analysis that bypasses the limit of a compressible elasticity solution. The works of Chan and Carlson (1970), Hill (1973b), Fosdick (1971) and Selvadurai and Spencer (1972) will be used in the present approach. We will denote by r and z the material coordinates in the radial and the vertical directions, respectively. The first step in this case is to establish the first-order solution, using a displacement potential $\psi(r,z)$:

$$\upsilon_r = \frac{z}{4\pi\mu}\frac{\partial\psi}{\partial r}, \tag{15}$$

$$\upsilon_z = -\frac{1}{4\pi\mu}\left[\psi - z\frac{\partial\psi}{\partial z}\right]. \tag{16}$$

The function $\psi(r,z)$ must be harmonic:

$$\nabla^2\psi = \left(\frac{\partial^2}{\partial r^2} + \frac{1}{r}\frac{\partial}{\partial} + \frac{\partial^2}{\partial z^2}\right)\psi = 0. \tag{17}$$

The hydrostatic pressure is

$$p_H(r,z) = \frac{\sigma_{rr} + \sigma_{zz} + \sigma_{\theta\theta}}{3} = \frac{1}{2\pi}\frac{\partial\psi}{\partial z} \tag{18}$$

and the corresponding Cauchy stresses are

$$\sigma_{rr} = p_H - \frac{z}{2\pi}\frac{\partial^2\psi}{\partial r^2}, \quad \sigma_{zz} = p_H - \frac{z}{2\pi}\frac{\partial^2\psi}{\partial z^2}, \quad \sigma_{\theta\theta} = p_H - \frac{z}{r}\frac{\partial\psi}{\partial r}, \quad \sigma_{r\theta} = -\frac{z}{2\pi}\frac{\partial^2\psi}{\partial r\partial z}. \tag{19}$$

Note that at the surface ($z = 0$)

$$\upsilon_r(r,0) = 0, \quad \upsilon_z(r,0) = -\frac{1}{4\pi\mu}\psi|_{z=0}, \tag{20}$$

$$\sigma_{\theta\theta}(r,0) = \sigma_{rr}(r,0) = \sigma_{zz}(r,0) = p_H|_{z=0}, \quad \sigma_{r\theta}(r,0) = 0. \tag{21}$$

The results indicate that the first-order solution at the surface predicts a deformation gradient of pure rotation. The first-order solution satisfies the Signiorini compatibility condition (Hill, 1973a). Far away from the contact region, the solution should tend to the results of a concentrated point force P acting along the z-direction. In this case, the function ψ is given by

$$\psi(r,z) = \frac{P}{(r^2 + z^2)^{1/2}}. \tag{22}$$

At the surface: $\partial\upsilon_z/\partial x_j\upsilon_j = 0$, $\partial\upsilon_z/\partial z = 0$, $\partial^2\upsilon_z/\partial x_j\upsilon_j = 0$, $\partial\upsilon_z/\partial x_k = -\partial\upsilon_k/\partial z$. Then, these conditions lead to absence of second-order normal stresses, provided that the strain energy density function is a symmetric function of the principal strain invariants, $W(I_1,I_2) = W(I_2,I_1)$, as for example the particular form of the Mooney–Rivlin case shown by Eq. (11). Using the particular form of Eq. (11), we can compute the second-order displacements at the surface. After some extensive calculations, we obtain

$$w_r(r,0) = -\frac{1}{(4\pi\mu)^2}\left[\psi\frac{\partial\psi}{\partial r}\right]_{z=0}, \quad w_z(r,0) = 0, \tag{23}$$

indicating that the first-order vertical surface displacements are retained to second order. The above analysis confirms that the macroscopic results found by Eqs. (13) and (14) hold true within the

context of the second-order analysis and for the particular form of the Mooney–Rivlin model (11).

From the previous analysis, Eq. (23), the surface deformation ($z = 0$) is the same as that of the first-order analysis

$$u_z = \left(\frac{\pi}{2} - \frac{r}{\alpha}\right)\alpha\tan\phi \quad (r \leqslant \alpha), \tag{24a}$$

$$u_z = \left(\sin^{-1}\frac{\alpha}{r} + \left(\frac{r^2}{\alpha^2} - 1\right)^{1/2} - \frac{r}{\alpha}\right)\alpha\tan\phi \quad (r > \alpha), \tag{24b}$$

where r, α denote the material radial coordinate and the projected contact radius to the horizontal surface. In the absence of surface stretching, the second-order contact pressure is essentially a second Piola–Kirchhoff stress (Cauchy stress rotated by the angle ϕ from cone geometry):

$$t_{zz} = -\frac{4}{6}E\tan\phi\cosh^{-1}\left(\frac{\alpha}{r}\right). \tag{25}$$

If we integrate the in the region, we obtain the total load as a function of, confirming the macroscopic result of Eq. (14), that is $C = P/D^2 \approx C_0$.

3. Finite element analysis

3.1. Basic considerations

We will distinguish the material (R,Z) and the current (r,z) coordinates, using the displacements

$$r = R + u_r(R,Z) \quad \text{and} \quad z = Z + u_z(R,Z). \tag{26}$$

The projected contact radius in the undeformed configuration is A $(0 \leqslant A < \sqrt{P/\mu})$. In the deformed configuration, the projected contact radius is

$$\alpha = A + u_r(A,0). \tag{27}$$

In the contact area $(0 \leqslant R < A, Z = 0)$, the deformation is described as

$$u_z(R,0) = D - (R + u_r(R,0))\tan\phi. \tag{28}$$

At the tip of the cone, the vertical displacement is D and the radial displacement is zero. At the contact perimeter, the amount of sinking-in is $u_z(A,0) = D - \alpha\tan\phi$. In the contact area, the Cauchy (true) stresses are constrained

$$\sigma_{rz}(R,0) = \frac{\sigma_{rr} - \sigma_{zz}}{2}\sin(2\phi) \tag{29}$$

due to the assumed frictionless contact and

$$\sigma_{rz}(R,0)\sin(2\phi) = p_N - (\sigma_{rr}\sin^2\phi + \sigma_{zz}\cos^2\phi) \tag{30}$$

due to the adhesionless contact where the contact pressure $p_N \leqslant 0$. Outside the contact area $(R \geqslant A,\ Z = 0)$

$$\sigma_{rr}(R,0) = \sigma_{zz}(R,0) = \sigma_{rz}(R,0) = 0. \tag{31}$$

Along the axisymmetry line $(R = 0)$, the angle of rotation is zero. In the frictionless case, this would lead to the relation $\partial u_r/\partial r \to +\infty$. In the case of friction, $\partial u_r/\partial z = \partial u_z/\partial r < 0$. Both of these results were verified by the finite element calculations. Also, along the axisymmetry line, $u_r(0,Z) = 0$. The far field solution is given by the point force incompressible linear elasticity. According to Kikuchi and Oden (1988), the problem can be solved by minimization of the energy function

$$\begin{aligned}\Pi = 2\pi\int_0^{+\infty}\int_0^{+\infty} WR\,\mathrm{d}R\,\mathrm{d}Z + 2\pi\int_0^{A}[&(\sigma_{rr}(R,0)\sin\phi \\ &+ \sigma_{rz}(R,0)\cos\phi)u_r(R,0) + (\sigma_{rz}(R,0)\sin\phi \\ &+ \sigma_{zz}(R,0)\cos\phi)u_z(R,0)]R\,\mathrm{d}R,\end{aligned} \tag{32}$$

where W is the strain energy density function. The existence of the solution is discussed by Curnier et al. (1992) and Ciarlet (1988). The finite element analysis will be based on the computational procedures described by Wriggers (2006). Due to linearity of the contact surface, the positive definiteness of the local tangent stiffness is guaranteed. We investigated three classic strain energy density functions: the Mooney–Rivlin, the Gent and the simple Ogden models.

The well-known Mooney–Rivlin model (Mooney, 1940) is valid up to moderate levels of strain. This model has been proven adequate for modeling uniaxial strains in tension and compression up to 45%. Its explicit relation with the strain invariants is

$$W = c_1(I_1 - 3) + c_2(I_2 - 3), \tag{33}$$

where c_1 and c_2 are constants (Pa) with $c_1 + c_2 > 0$. If $c_2 = 0$ (highly swollen rubbers), the model reduces to the Neo-Hookean one. The shear modulus at zero straining is $\mu = 2(c_1 + c_2)$. An excellent discussion on the origin of the c_2 term in rubber elasticity has been given by Waggner (1994), who proved that it is due to the non-affined deformation of the entanglement network due to the increasing lateral restriction of the neighboring molecular chains. For small values of c_1 (e.g. less than 0.1 MPa for natural rubber), $c_1 = c_2$.

To investigate the influence of a limiting value for the first strain invariant (i.e. the existence of a locking stretch in uniaxial tension, $\lambda_L > 1$), we examined a simple strain energy density suggested by Gent (2005)

$$W = -\frac{\mu J_m}{2}\ln\left(1 - \frac{J_1}{J_m}\right), \tag{34}$$

where $\mu > 0$ is the shear modulus at zero straining and J_m is the maximum value of J_1 and depends on the uniaxial locking stretch as $J_m = (2\lambda_L^4 + 1)/(\lambda_L^2) - 3$. For large values of the locking stretch, $\lambda_L \to +\infty$, the model reduces to the Neo-Hookean model. Similar to Gent, there are other models (e.g. Arruda and Boyce, 1993) that capture well the characteristic S-shaped load versus stretch curve in uniaxial tension tests, involving locking stretches of 2–3. The present model was selected for simplicity in order to investigate the basic response.

A simple model that can also capture the S-shape response of uniaxial tests (without the locking stretch) is the simple Ogden model

$$W = \frac{2\mu}{\zeta^2}(\lambda_1^\zeta + \lambda_2^\zeta + \lambda_3^\zeta - 3), \tag{35}$$

where $\mu > 0$ is the shear modulus at zero straining and $\zeta > 1$ is the power law constant that controls the S-shape of the uniaxial tension response. Note that for $\zeta = 2$, the model reduces to the Neo-Hookean model.

Following Hill (1973a), we can find the exact expressions of the principal Cauchy stresses in the undeformed configuration. Denote by

$$\lambda = 1 + u_r/R \quad \text{and} \quad I = I_1 - \lambda^2. \tag{36}$$

Then, the principal stresses are the ones in the plane (r,z) and the hoop stresses

$$\sigma_{1,3} = p + \left(I \pm \sqrt{I^2 - \frac{4}{\lambda^2}}\right)\frac{\Phi}{2}, \tag{37}$$

$$\sigma_2 = \sigma_{\theta\theta} = p + \Psi\lambda^2. \tag{38}$$

In case of a Mooney–Rivlin material

$$\Phi = 2(c_1 + \lambda^2 c_2) \quad \text{and} \quad \Psi = 2(c_1 + (I - \lambda^{-4})c_2). \tag{39}$$

The hydrostatic pressure must be singular at the tip of the cone so that locally the stress state to be hydrostatic and have infinite principal planes (of zero shear traction). At the surface, outside the contact

region, the principal stresses in the (r,z) plane are zero, $\sigma_1 = \sigma_3 = 0$. Then, $I = 2/\lambda$, leading to $\sigma_{\theta\theta} = \sigma_2 = -p + \Phi I/2$ and $p = \Phi I/2$.

The angle of rotation ξ is given by

$$\tan\xi = \frac{\partial u_r/\partial z - \partial u_z/\partial r}{2 - \partial u_r/\partial r - \partial u_z/\partial z}. \tag{40}$$

As we approach the cone tip, a singularity of $\partial u_r/\partial r$ arises and (40) gives two angles of rotation, depending on how we approach the cone-tip: $\xi \to \phi$ as $Z = 0$ and $R \to 0-$, $\xi \to 0$ as $R = 0$ and $Z \to 0-$.

We have implemented the above strain energy density functions to the ANSYS finite element code (ANSYS, 2006), with 4-noded axisymmetric, hybrid elements, with bi-linear isoparametric interpolation for the incremental displacement field, in conjunction with constant hydrostatic pressure and constant dilatation over the current configuration. The deformation gradient is split into volume preserving and dilatational parts. The mixed formulation is constructed based on the linear Hu-Washizu principle method, as suggested by Simo et al. (1985). The cone indentor was modeled as a rigid surface. The cone angles were 140.6° (corresponding to the well-known Vickers indentation test), 120° and 60°. The finite element mesh is shown in Fig. 2. The outer boundaries of the mesh was chosen to be at least 20 times the maximum contact radius, $A \approx 20\sqrt{P/\mu}$. The boundary conditions are shown in Fig. 1 as rollers. We have used 40,187 to 53,611 elements, with 90–130 elements resolving the contact region at maximum load. The loading was applied in 200 equal displacement steps and required 2–3 iterations per load step, with standard Newton–Raphson procedure and convergence in the energy norm with a tolerance of 10^{-14}. Increasing the steps to 400, did not affect the results. The incompressibility tolerance was 10^{-7}. The Hughes procedure was used, taking the rotation matrix at half the loading step (Hughes, 1980). The Lagrange multiplier method was used for the normal contact and was enforced at all iterations, sacrificing speed for accuracy. The return mapping method was used for friction (Giannakopoulos, 1989). A full check for "hourglass" modes was performed at the end of each load step to be sure of the quality of the solution. Another check was made to confirm that the indentation depth and the contact radius were advancing monotonically with load.

3.2. Results of the frictionless analysis

We are interested in the macroscopic results, that is, the force-depth and the contact radius-depth relations. We report these results as ratios with the classic linear elasticity results, Eqs. (13) and (14), that were proven for the particular Money–Rivlin model (in the FEM model we used Eq. 33). Table 1 summarizes the results for a cone angle of 140.6° (equivalent to the well-known Vickers pyramid indentor) indenting a Mooney–Rivlin material. The principal stretches at the cone tip are extreme and are also reported in Table 1. The maximum stretch is in the radial direction, followed by the circumferential direction. The smallest stretch is in the vertical direction, as expected. It is clear that the strains are of the order of 50%, in the range that the Mooney–Rivlin model is valid. It is astonishing to find that, although the problem predicts large strains, the analytic linear elasticity works for all types of Mooney–Rivlin materials within more than 95% accuracy. It is also astonishing to observe that the strains are almost invariants for any combination of the ratio $c_1/(c_1 + c_2)$. The above conclusions hold for blunt cones, as is evident from Tables 2 and 3 that report similar quantities for cone angles of 120° and 60° (equivalent to the well-known Rockwell indentor). In this case, the strains are increased dramatically and the Mooney–Rivlin model may not be appropriate. Finally, the analysis showed that the constant $c_2 > 0$, otherwise there cannot be any solution for the indentation problem.

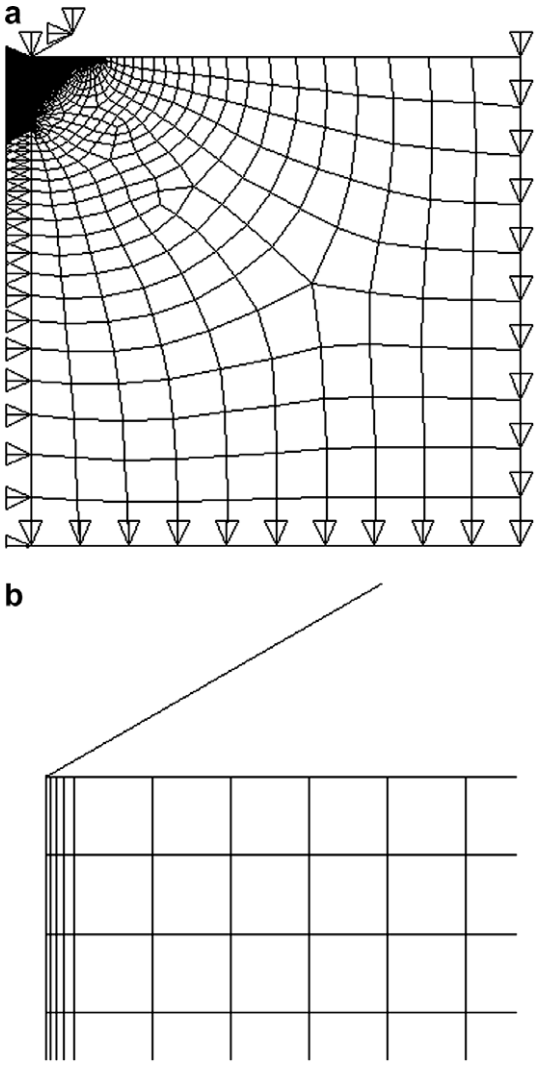

Fig. 2. (a) Overall view of the finite element mesh used in the analysis. The dark area corresponds to a very fine uniform mesh. The triangles denote rolling constraints, with line of rolling the free side of the triangle. (b) Mesh refinement alongside the axis of symmetry.

Table 1
Material model: Mooney–Rivlin. Friction coefficient: 0. Cone angle: 140.6°.

$c_1/(c_1+c_2)$	C/C_0	α/α_0	Stretches at the cone-tip		
			λ_1	λ_2	λ_3
0.2765	1.0502	1.0189	1.4227	1.3836	0.5099
0.5000	1.0357	1.0264	1.4237	1.3850	0.5091
0.7234	1.0210	1.0377	1.4244	1.3862	0.5085
0.9985	1.0025	1.0472	1.4245	1.3874	0.5083

Table 2
Material model: Mooney–Rivlin. Friction coefficient: 0. Cone angle: 120°.

$c_1/(c_1+c_2)$	C/C_0	α/α_0	Stretches at the cone-tip		
			λ_1	λ_2	λ_3
0.2765	1.0527	1.0242	2.2610	2.0282	0.2181
0.5000	1.0308	1.0364	2.3089	2.0686	0.2093
0.7234	1.0069	1.0424	2.3800	2.1291	0.1973
0.9985	0.9763	1.0515	2.5738	2.2964	0.1691

Table 3
Material model: Mooney–Rivlin. Friction coefficient: 0. Cone angle: 60°.

$c_1/(c_1+c_2)$	C/C_0	α/α_0	Stretches at the cone-tip		
			λ_1	λ_2	λ_3
0.2765	1.2009	1.1273	8.8375	4.4371	0.0256
0.5000	1.1299	1.1455	9.3092	4.6693	0.0231
0.7234	1.0482	1.1455	10.135	5.0784	0.0195
0.9985	0.9047	1.1591	20.227	10.115	0.0049

Table 4
Material model: Gent. Friction coefficient: 0. Cone angle: 140.6°.

λ_L	C/C_0	α/α_0	Stretches at the cone-tip		
			λ_1	λ_2	λ_3
2.75	1.0069	1.0377	1.4206	1.3803	0.5115
2.25	1.0105	1.0377	1.4146	1.3422	0.5163
1.75	1.0229	1.0189	1.3732	1.3208	0.5516
1.20	1.0472	1.0170	1.2744	1.2461	0.6347
1.11	1.0988	0.9811	1.1988	1.1766	0.7191

To investigate the influence of the locking stretch, λ_L, we used the Gent model. Table 4 summarizes the results for a cone angle of 140.6°. It is surprising to find once more that the macroscopic response follows linear elasticity, even for rather low locking stretches. In this case, the results are almost indistinguishable from those predicted by the Mooney–Rivlin model. For very low locking stretches (below 1.2), the indentation response becomes stiffer and the stretches try to become equal.

Table 5
Material model: Ogden. Friction coefficient: 0. Cone angle: 140.6°.

ζ	C/C_0	α/α_0	Stretches at the cone-tip		
			λ_1	λ_2	λ_3
0.5	1.0236	1.0185	1.498	1.435	0.486
1.5	1.009	1.0185	1.497	1.432	0.487
2.5	0.9962	1.0288	1.497	1.428	0.490
3.5	0.9849	1.0288	1.495	1.423	0.491

Table 6
Material model: Ogden. Friction coefficient: 0. Cone angle: 120°.

ζ	C/C_0	α/α_0	Stretches at the cone-tip		
			λ_1	λ_2	λ_3
0.5	1.0066	1.0438	4.128	3.578	0.114
1.5	0.9852	1.0522	3.162	2.742	0.156
2.5	0.9682	1.0606	2.796	2.424	0.185
3.5	0.9553	1.0606	2.589	2.245	0.207

Tables 5 and 6 present the macroscopic results, that is, the force-depth and the contact radius-depth relations for the simple Ogden model, for different values of the parameter ζ. We report these results as ratios with the classic linear elasticity results, Eqs. (13) and (14), for cone angles 140.6° and 120°, respectively. It is astonishing to observe that for cone angles 140.6° the strains are almost invariants for any value of the parameter ζ and agree closely to those of the Mooney–Rivlin model. For cone angles of 120° the strains are increasing dramatically with decreasing ζ.

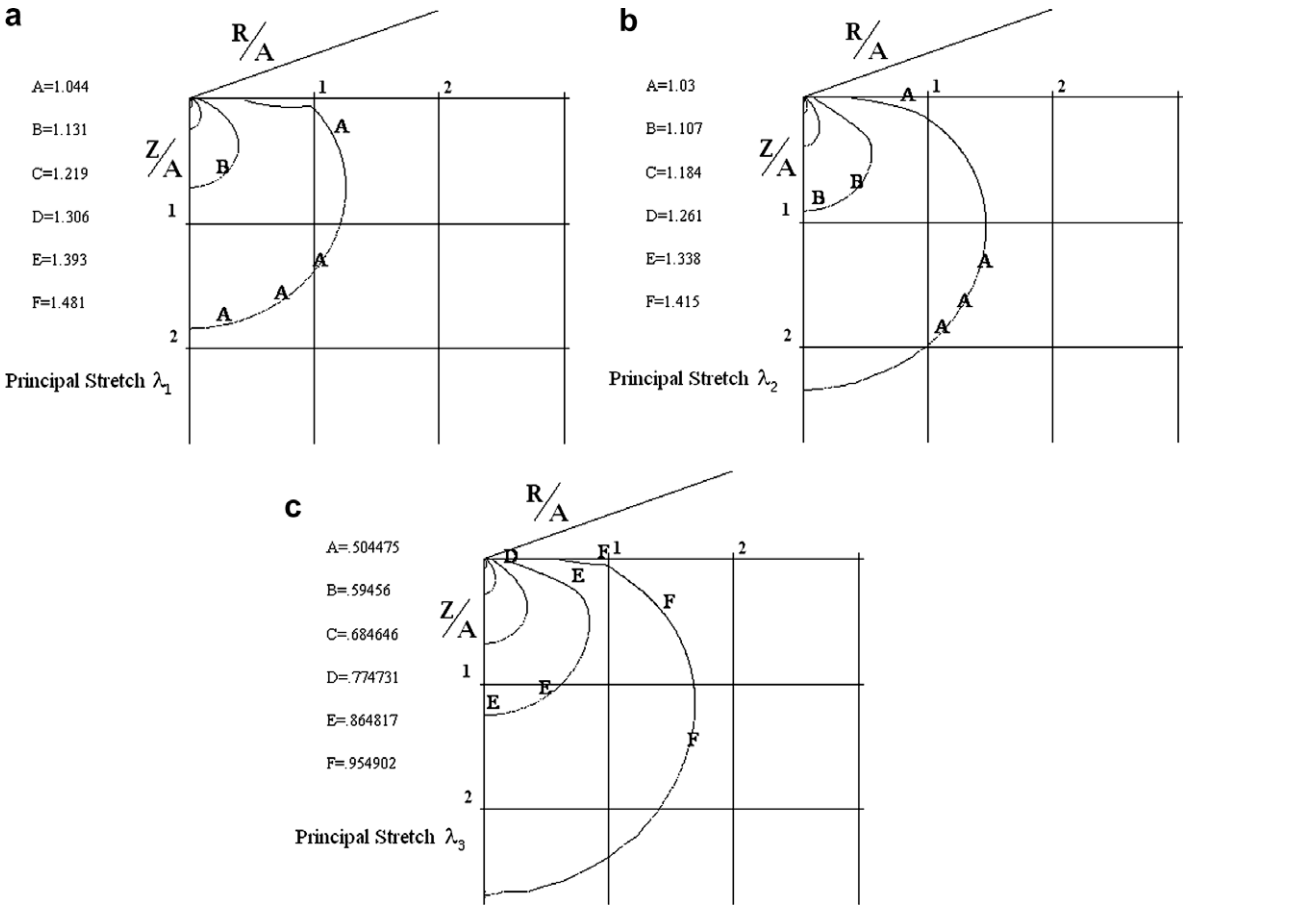

Fig. 3. Isobars of the principal stretches for the Mooney–Rivlin model, frictionless case and cone angle 140.6°. The contour plots are in the normalized reference configuration (R/A, Z/A), where A is the reference contact radius.

Some further results of the basic form of the Mooney–Rivlin model are worth presenting. In Fig. 3, the isobars of the stretches λ_1, λ_2 and λ_3 were plotted in the undeformed configuration for cone angle of 140.6°. Due to incompressibility, $\lambda_1\lambda_2\lambda_3 = 1$, as expected. The stretches are bounded from the far-field expected value of 1 and the maximum values at the cone-tip (which are finite). The results are almost the same for any ratio $c_1/(c_1 + c_2)$. The finite element results indicate that the deviatoric Cauchy stresses are finite everywhere and the pressure exhibits singularity at the cone-tip. The deviatoric stresses in the radial and the circumferential direction are nearly proportional with the Lagrangian strains. The calculations showed that Fig. 3 is almost the same for all Ogden models, as well as for the Gent models with sufficiently large locking stretch (>1.7).

Another revealing figure is Fig. 4, which shows the maximum principal stretch λ_1, along the contact radius, at the surface ($Z = 0$) for cone angles 140.6° and 120°. The material radial distance R is normalized by the corresponding reference contact radius A. Note that outside the contact region, the principal stretch approaches the far-field value of 1, as expected. The distributions for the two cone angles are similar; however, the values are higher for the sharper indenter. We can conclude that for the Mooney–Rivlin model, the surface is extended a lot as the cone angle is decreasing, suggesting a possible puncturing of the surface.

Fig. 5 shows the radial displacement, u_r, at the surface ($Z = 0$) for cone angles 140.6° and 120° and for all material properties of the Mooney–Rivlin model shown in Tables 1 and 2. Both the material radial coordinate and the radial displacement are normalized by the corresponding material contact radius A. The radial displacements take negative values in the outer contact region and they are zero at two points of the contact region: R/A=0 and $R/A \approx 0.8 \div 0.9$. Far away from the contact region, $R/A > 7$, the radial displacement approaches the far-field value of 0, as expected. The radial displacement distributions are similar and depend on the cone angle and the ratio $c_1/(c_1 + c_2)$. The radial displacement distribution takes the limiting value 0, as the cone angle approaches 180° and increases in amplitude as the cone angle decreases.

Fig. 6 shows the vertical displacement, u_z, at the surface ($Z = 0$) for cone angles 140.6° and 120° and for all material models shown in Tables 1–6. Both the material radial coordinate and the vertical displacement are normalized by the corresponding material contact radius A. Far away from the contact region, $R/A > 7$, the vertical displacement approaches the far-field value of 0, as expected. It is very interesting to find that the vertical displacement distributions are almost similar and depend basically on the cone angle. The figure also includes the linear elasticity prediction of Eq. (24), which fits all the results very well, confirming the validity of the second order theoretical approximation.

Turning our attention to the contact pressure, we show in Fig. 7 the first Piola–Kirchhoff contact pressure for cone angle 140.6°,

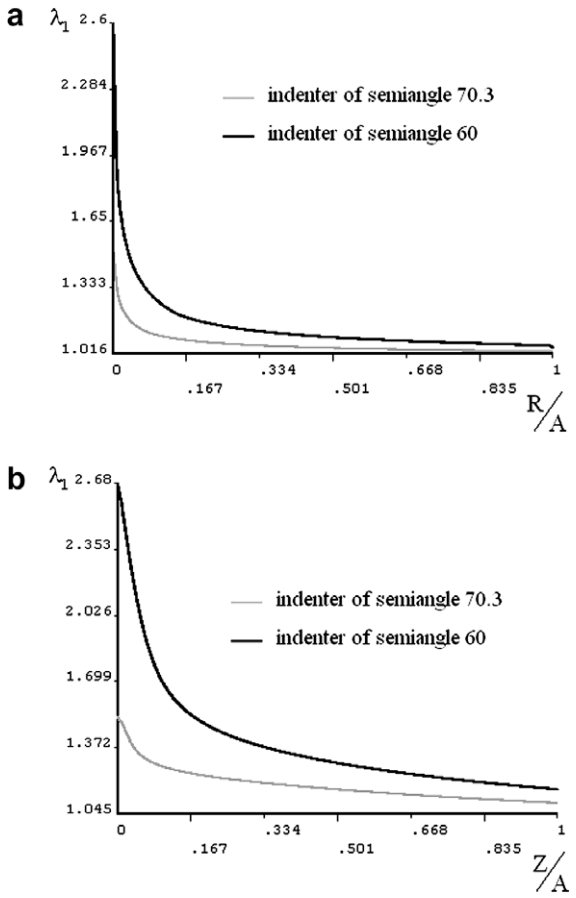

Fig. 4. (a) The maximum principal stretch along the contact radius, at the surface, for two different cone angles (140.6° and 120°) and for the Mooney–Rivlin model. (b) The maximum principal stretch along the axis of symmetry, for the same cone angles and material model. The material radial direction R and axial direction Z are normalized by the material contact radius A.

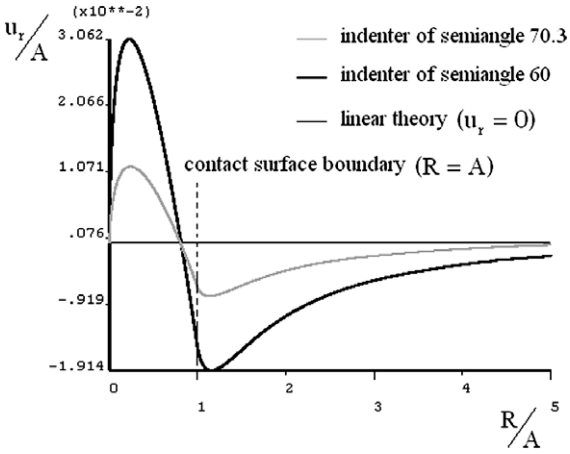

Fig. 5. The radial displacement along the contact radius, at the surface, for two different cone angles (140.6° and 120°) and for the Mooney–Rivlin model. Both the material radial direction R and the radial displacement are normalized by the material contact radius A.

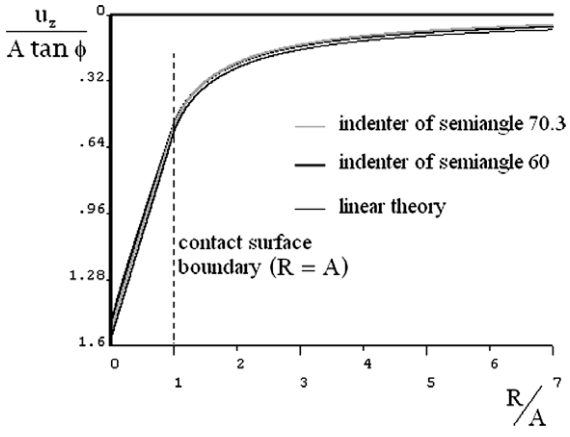

Fig. 6. Normalized vertical displacement as a function of the normalized reference radial direction. The normalizing length is the reference contact radius A.

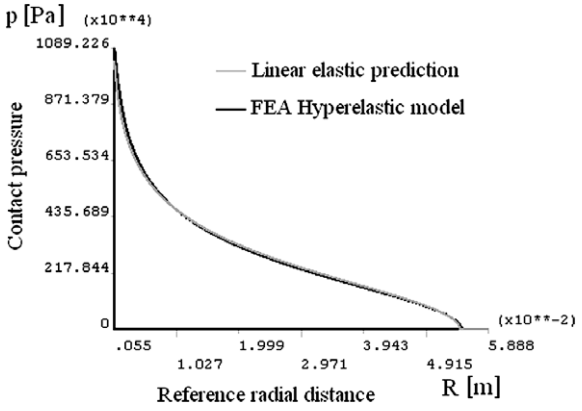

Fig. 7. The first Piola–Kirchhoff contact pressure, for cone angle 140.6° and for the Mooney–Rivlin model. The prediction of linear elasticity is also shown. In this case, $P = 18.5$ kN and $E = 7.5$ MPa.

applied force $P = 18.5$ kN and Mooney–Rivlin material with $\sqrt{P/\mu} = 8.2$ cm. The prediction of the linear elasticity is also shown in Fig. 7. It is clear that the linear elasticity approximation is good. However, the asymptotic nature of the contact pressure close to the cone-tip was investigated in more detail.

Fig. 8 shows the normalized true contact pressure p_N/μ versus the normalized material radius R/A for cone angles of 140.6° and 120°. Fig. 8a gives the results in a semi-logarithmic plot, whereas Fig. 8b gives the results in a log–log plot. From these figures, we can conclude that the logarithmic singularity dominates in blunt cone (140.6°) indentations and power-law singularity dominates in sharp cone (120°) indentations.

Fig. 9 shows the principal directions of the stretches on the deformed configuration for sharp cone (120°) indentation of the Mooney–Rivlin material. Note that close to the cone-tip, there is a double value of the angle of rotation $(0, \phi)$ and, as expected, the rotation matrix is not single valued. The rest of the material points have unique angle of rotation.

Fig. 10 shows the isobars of the hydrostatic pressure, normalized to the initial modulus μ, in the reference configuration, normalized by the corresponding material contact radius A. For blunt cones (140.6°), the results are almost invariant of the model (except for the Gent model with low locking stretches) and a typical result is given in Fig. 10a for the Mooney–Rivlin model. For sharp cones (120°), the results change drastically with the material parameters, as shown in Fig. 10b for the Gent model with locking stretch 1.2.

3.3. Effects of friction

The friction between the indentor and the elastomer is a complex physical phenomenon, Person (2000). Friction depends on the contact velocity and the temperature. In the present analysis we were confined on the simple Coulomb type of friction that depends on the surface displacements and the contact tractions. Typical values of the dry friction coefficient between metal and rubber is 0.15–4.00. In the present analysis we used values of friction 0.2, 1 and 10. For sufficiently high friction coefficient, the surface sticks completely at the indentor. In this case, the stress singularity at the cone tip changes significantly (Keer and Parihar, 1978). Schallamach (1971) showed that surface instability causes wrinkles on the surface of soft rubber which undergoes frictional sliding. Best et al. (1981) investigated the origin of Schallamach's waves and showed

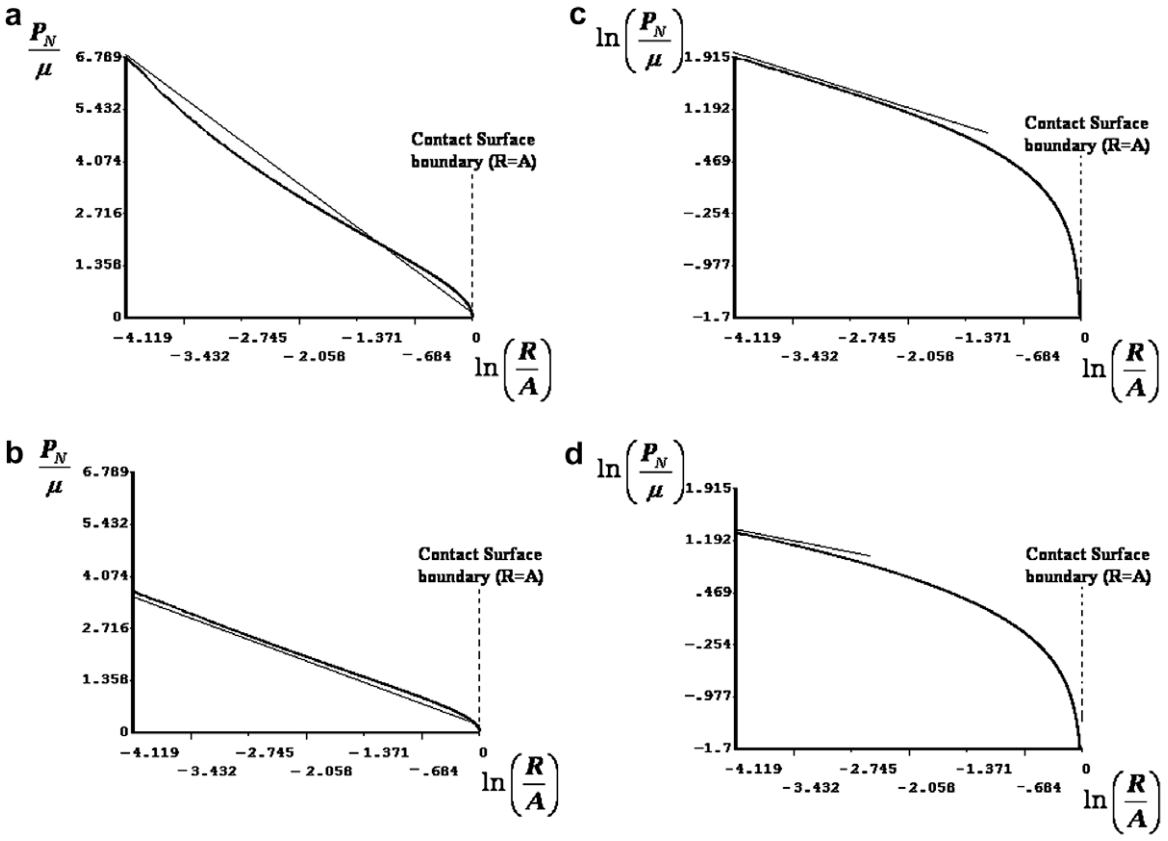

Fig. 8. Investigation of the cone-tip asymptotic behavior of the true contact presure, for cone angles 140.6° and 120° and for the Mooney–Rivlin model. The contact pressure is normalized by the shear modulus and the material radius by the contact radius in the undeformed configuration. (a) Semi-logarithmic plot for cone angle 120°. (b) Semi-logarithmic plot for cone angle 140.6°. (c) Log–log plot for cone angle 120°. (d) Log–log plot for cone angle 140.6°.

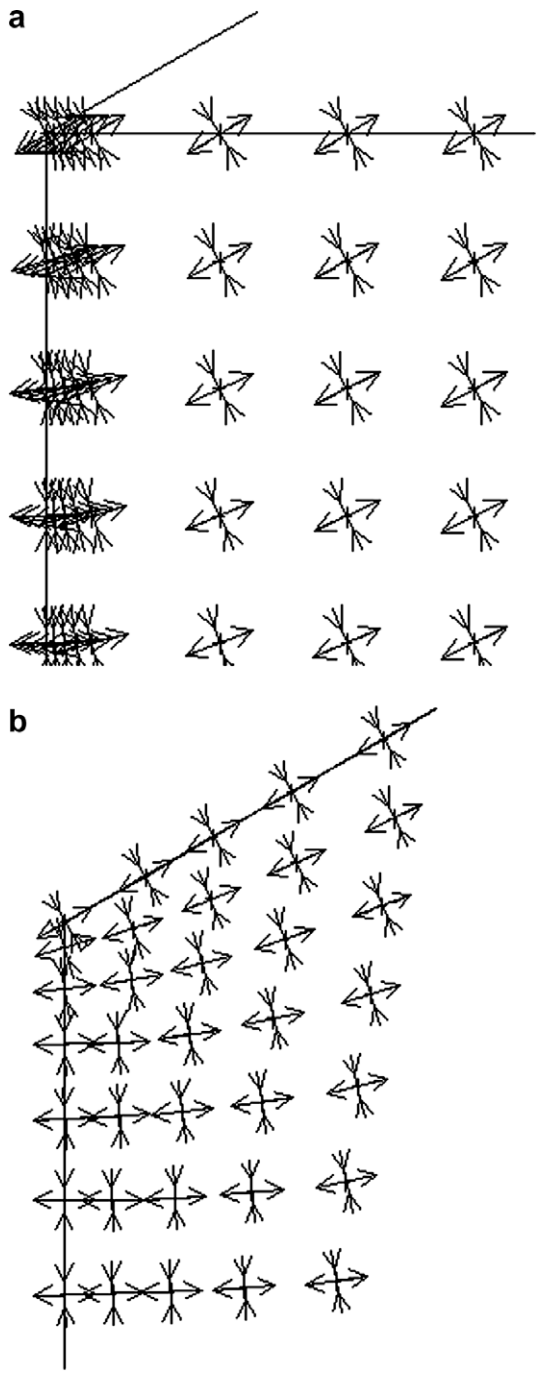

Fig. 9. Principal stretch directions for the Mooney–Rivlin model. (a) Reference configuration. (b) Deformed configuration. The cone angle is 120°. The friction coefficient is 0.0. In this case, P = 18.5 kN and E = 7.5 MPa.

that they can explained as instability of the surface due to high compressive strains tangential to the surface. They used the Mooney–Rivlin model and found a critical surface stretch of 0.54. As was clear from the finite element calculations, such surface (compressive) strains were never encountered in our solutions, even for very high friction coefficients.

Some further results of the basic form of the Mooney–Rivlin model are worth presenting. Fig. 11 shows the first Piola–Kirchhoff contact pressure for cone angle 140.6°, applied force P = 18.5 kN and Mooney–Rivlin material with $\sqrt{P/\mu} = 8.2$ cm. The results include friction coefficients 0.0, 0.2, 1.0 and 10.0. It is interesting to note that no appreciable difference was detected, indicating the macroscopic results (force-depth and depth-radius) for the cone angle 140.6° are not influenced by friction. The macroscopic results for sharp cones (60°), however, are influenced by friction, as shown clearly in Table 7. The presence of friction reduces the contact radius and increases the contact stiffness, however, these effects level for friction coefficient greater than 1.

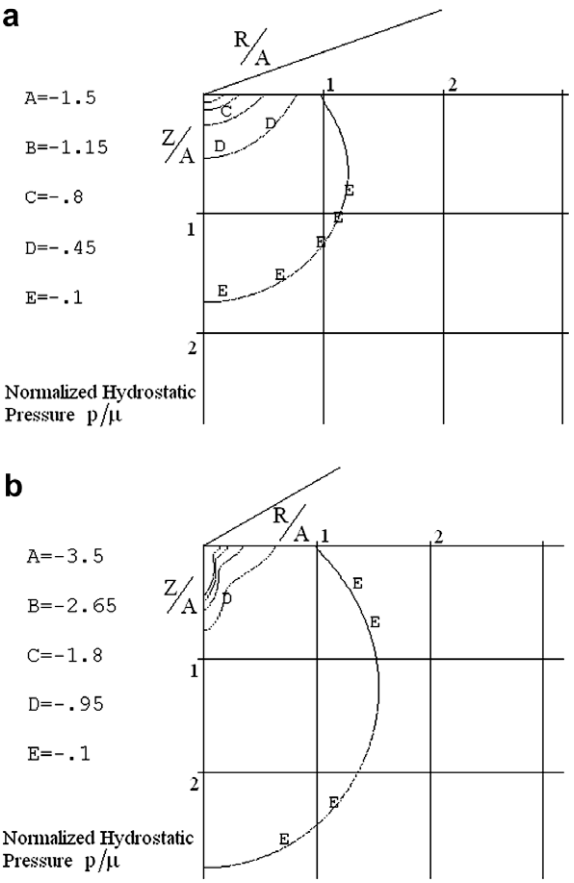

Fig. 10. Hydrostatic pressure normalized by the initial shear modulus. The contour plots are in the normalized reference configuration (R/A, Z/A). (a) Mooney–Rivlin model and cone angle 140.6°. (b) Gent model (λ_L = 1.2) and cone angle 120°. The friction coefficient is 0.0. In this case, P = 18.5 kN and E = 7.5 MPa.

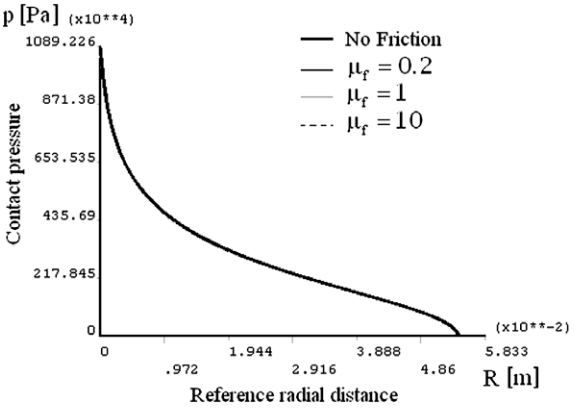

Fig. 11. The first Piola–Kirchhoff contact pressure, for cone angle 140.6° and for the Mooney–Rivlin model. The results include friction coefficients 0.0, 0.2, 1.0 and 10.0. In this case, P = 18.5 kN and E = 7.5 MPa.

Table 7
Material model: Mooney–Rivlin, $c_1/(c_1 + c_2) = 0.5$. Cone angle: 60°.

Friction coefficient	C/C_0	α/α_0
0.00	1.1299	1.1455
0.20	1.1783	0.9749
1.00	1.1908	0.9641
10.0	1.1911	0.9636

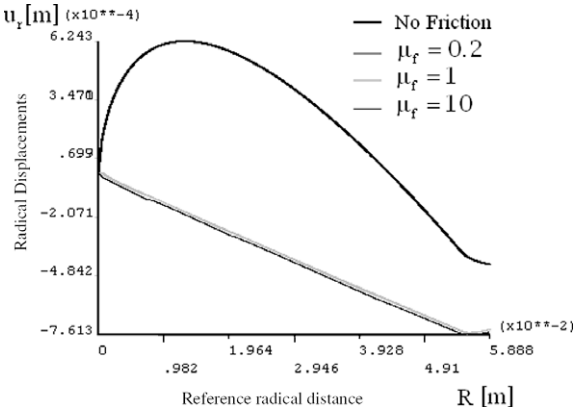

Fig. 12. The radial displacement along the contact radius, at the surface, for cone angle 140.6° and for the Mooney–Rivlin model. The results include friction coefficients 0.0, 0.2, 1.0 and 10.0. In this case, $P = 18.5$ kN and $E = 7.5$ MPa. All curves with friction coefficient greater than 0.0 are almost identical.

Fig. 12 shows the radial displacement for cone angle 140.6°, applied force $P = 18.5$ kN and Mooney–Rivlin material with $\sqrt{P/\mu} = 8.2$ cm. The analysis examined friction coefficients 0.0, 0.2, 1.0 and 10.0. The results show that even for moderate friction coefficients the surface sticks on the cone and the surface radial deformation is negative. Contrary to the frictionless case where $\partial u_r/\partial r \to +\infty$ at the cone-tip, the presence of friction results to a finite value of $\partial u_r/\partial r$ at the cone-tip. As a result, the angle of rotation at the cone-tip is unique, $\xi = 0$. Recall that the frictionless case predicts two values of angle of rotation at the cone tip, $\xi = 0$ and $\xi = \phi$, depending on how the cone-tip is approached (see also discussion of Eq. (40)).

Fig. 13 shows the principal directions of the stretches on the deformed configuration for sharp cone (120°) indentation of the Mooney–Rivlin material, for friction coefficient 1. Note that close to the cone-tip, there is a single value of the angle of rotation (zero) and, as expected, the rotation matrix is single valued.

Fig. 14 shows the maximum principal stretch λ_1, along the contact radius, at the surface ($Z = 0$) for cone angle 140.6°. The material radial distance R is normalized by the corresponding reference contact radius A. Note that outside the contact region, the principal stretch approaches the far-field value of 1, as expected. The stretch distributions for friction coefficients 0.2, 1.0 and 10.0 are almost the same. In comparison with the frictionless case, the stretch is strongly decreasing in the region $0 \leqslant R/A < 0.8$ and is mildly increasing in the region $R/A > 0.8$. Lim and Chaudhri (2004) took into account friction through the form[1] $C/C_0 = 1 + \mu_f \tan\phi$, suggesting a linear dependence of the contact stiffness with the Coulomb friction coefficient μ_f.

This was not confirmed by the present analysis. Although friction indeed leads to the increase of the contact stiffness, the influence of the friction constant has a non-linear dependence on the contact stiffness and approaches a plateau for very high values of the friction coefficient (perfect stick condition).

It is very interesting to note that Eq. (24) fits well the surface vertical displacements predicted by finite elements, regardless of the material model and friction, for cone angles larger than 90°.

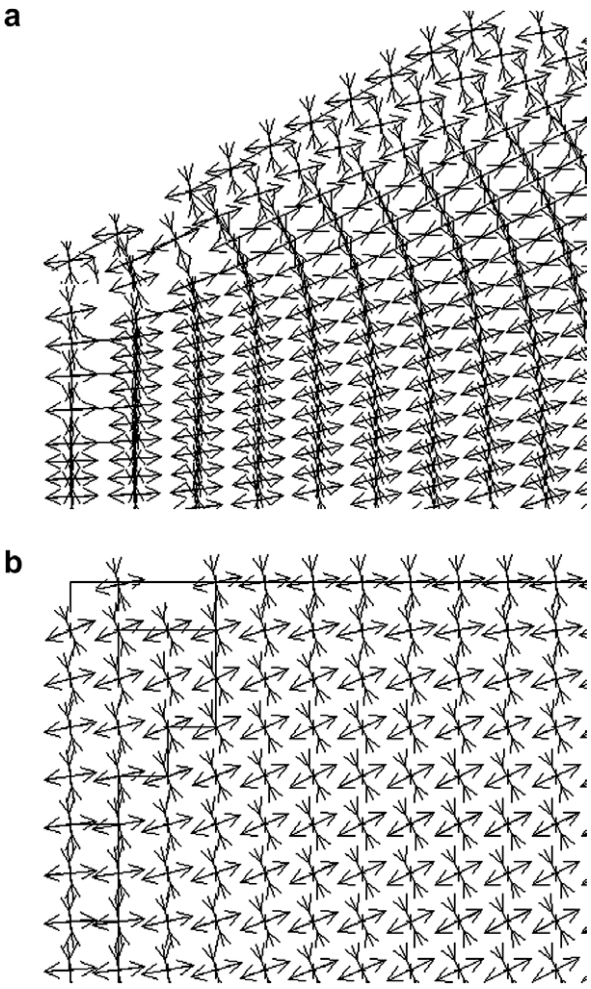

Fig. 13. Principal stretch directions for the Mooney–Rivlin model. (a) Reference configuration. (b) Deformed configuration. The cone angle is 120°. The friction coefficient is 1.0. In this case, $P = 18.5$ kN and $E = 7.5$ MPa.

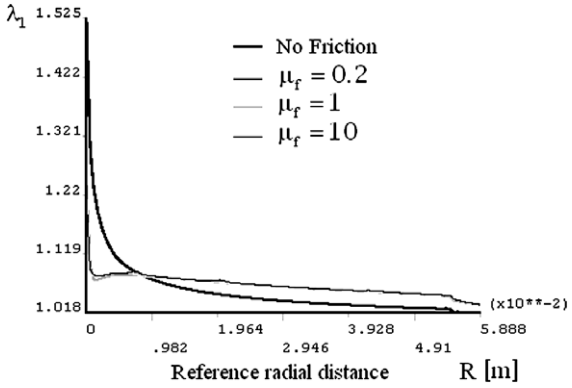

Fig. 14. The maximum principal stretch along the surface, for cone angle 140.6° and for the Mooney–Rivlin model. The results include friction coefficients 0.0, 0.2, 1.0 and 10.0. In this case, $P = 18.5$ kN and E=7.5 MPa. All curves with friction coefficient greater than 0.0 are almost identical.

[1] Recall that $C = P/D^2$ for the hyperelastic response including friction effect and C_0 is P/D^2 for the linear elastic response without friction (Eq. (14)).

Deviations appear for the low-locking-stretch Gent model. For cone angles smaller than 90°, the surface deformation deviates from the prediction of (24).

4. Conclusions

We have analyzed the indentation of incompressible rubber materials by rigid cone and we found a set of analytic expressions that relate the indentation depth D with the applied vertical force P, the contact radius α and the angle φ. The dominant material parameter is the shear modulus μ at zero straining. For relatively blunt cones, the analysis predicts that the indentation response is very close to that predicted by linear elasticity. This unexpected (approximate) result seems to be independent of the strain energy density function, but is limited to blunt indentors. Our analytic results were of second order and were confirmed by finite elements. Instrumented indentation tests with blunt cones (Lim and Chaudhri, 2004) support the present findings. As we increase φ (sharper cones), the macroscopic force-depth response becomes stiffer and depends on the exact form of the strain energy density function. Friction plays a small role to the macroscopic response of the blunt indentors, but is very important for the sharp indentors.

It is not clear at this point whether the results for cone indentors apply to pyramid indentors such as Vickers, Berkovich and Knoop. We believe that the present results are approximately valid for such cases as well. Regarding blunt pyramid indentors, the second order analysis for the frictionless case leads to the linear elasticity solutions given by Giannakopoulos (2006). Giannakopoulos also showed experimentally that the imprint of a Knoop indentation on rubber follows the linear elasticity predictions.

We conclude that in order to solve the inverse problem, which is finding the shear modulus μ from the indentation test, we can use blunt cones and the results of linear elasticity. If we are interested in more details of the strain energy density function, we have to use sharper cones.

References

ANSYS Inc., 2006. University advanced version 10, Canonburg, PA 15317.

Antman, S.S., 1995. Nonlinear Problems of Elasticity. Springer, New York.

Arruda, E.M., Boyce, M.C., 1993. A three-dimensional constitutive model for the large stretch behavior of rubber elastic materials. J. Mech. Phys. Solids 41, 389–412.

ASTM D2240, 2003. Durometer Hardness.

Best, B., Meijers, P., Savkoor, A.R., 1981. The formation of Schallamach waves. Wear 65, 385–396.

Briscoe, B.J., Sebastian, K.S., Adams, M.J., 1994. The effect of indenter geometry on the elastic response to indentation. Journal of Physics D: Applied Physics 27, 1156–1162.

Brown, R., 2006. Physical Testing of Rubber, fourth ed. Springer Science and Business Media Inc., New York.

BS 903 Part A57, 1997. Determination of Indentation Hardness by Means of Pocket Hardness Meters.

Busfield, J.J.C., Thomas, A.G., 1999. Indentation tests on elastomer blocks. Rubber Chemistry and Technology 75, 876–894.

Chan, C., Carlson, D.E., 1970. Second order incompressible elastic torsion. International Journal of Engineering Science 8, 415–430.

Chang, W.V., Sun, S.C., 1991. Non-linear elastic analysis of the hardness test on rubber-like materials. Rubber Chemistry and Technology 64, 202–210.

Choi, I., Shield, R.T., 1981. Second order effects in problems for a class of elastic materials. Journal of Applied Mathematics and Physics (ZAMP) 32, 361–381.

Ciarlet, P.G., 1988. Mathematical Elasticity I: Three-dimensional Elasticity. North-Holland, Amsterdam.

Crawford, R.J., Stephens, G., 1985. Microhardness testing of plastics using ball and conical indenters. Polymer Testing 5, 113–136.

Curnier, A., He, Q.C., Telega, J.J., 1992. Formulation of unilateral contact between two elastic bodies undergoing finite deformation. Comptes Rendus de l'Académie des Sciences de Paris (série II.6 Méca.des Sol.), t. 314.

Davey, A.B., Payne, A.R., 1964. Rubber in Engineering Practice. Maclaren, London.

Eirich, F.R., 1978. Science and Technology of Rubber. Academic Press, New York.

Fosdick, R., 1971. Statically possible radially symmetric deformation in isotropic incompressible elastic solids. Journal of Applied Mathematics and Physics (ZAMP) 22, 590–607.

Fisher-Cripps, A.C., 2002. Nanoindentation. Springer, New York.

Fung, Y.C., 1993. Biomechanics: Mechanical Properties of Living Tissues, second ed. Springer, New York.

Fung, Y.C., 1994. A First Course in Continuum Mechanics for Physical and Biological Engineers and Scientists, third ed. Prentice-Hall, Englewood Cliffs, NJ.

Gao, Y.C., 2001. Asymptotic analysis of the nonlinear Boussinesq problem for a kind of incompressible rubber materials (compression case). Journal of Elasticity 64, 111–170.

Gao, Y.C., Mai, Y.-W., 2002. The contact problem of a rubber half-space dented bya rigid cone apex. Archive of Applied Mechanics 72, 213–228.

Gent, A.N., 1992. Engineering with Rubber. Hanser Press, New York.

Gent, A.N., 2005. Extensibility of rubber under different types of deformation. Journal of Rheology 49, 271–275.

Gent, A.N., Yeoh, O.H., 2006. Small indentations of rubber blocks: effect of size and shape of block and of lateral compression. Rubber Chemistry and Technology 79, 674–693.

Giannakopoulos, A.E., 1989. The return mapping method for the integration of friction constitutive relations. Computers and Structures 32, 57–168.

Giannakopoulos, A.E., 2006. Elastic and viscoelastic indentation of flat surfaces by pyramid indentors. Journal of the Mechanics and Physics of Solids 54, 1305–1332.

Green, A.E., Adkins, J.E., 1970. Large Elastic Deformations, second ed. Charendon Press, Oxford.

Greenwood, J.A., Tabor, D., 1958. The friction of hard sliders on lubricated rubber: the importance of deformation losses. Proceedings of the Physical Society 71, 989–1001.

Hill, J.M., 1973a. Partial solutions of finite elasticity. Axially symmetric deformations. Journal of Applied Mathematics and Physics (ZAMP) 24, 409–418.

Hill, J.M., 1973b. Notes on the paper by Chan, C. and Carlsson, D.E. Second order incompressible elastic torsion. International Journal of Engineering Science 11, 331–336.

Hughes, T.J.R., 1980. Generalization of selective integration procedures to anisotropic and nonlinear media. International Journal for Numerical Methods in Engineering 15, 1413–1418.

ISO 7619-I, 2004. Determination of Indentation Hardness-Durometer method (Shore Hardness).

ISO 7619-II, 2004. Determination of Indentation Hardness IRHD Pocket Hardness Meter.

Jabareen, M., Rubin, M.B., 2007. Hyperelasticity and physical shear buckling of a block predicted by the Cosserat point element compared with inelasticity and hourglassing predicted by other element formulation. Computational Mechanics 40, 447–459.

Johnson, K.L., 1985. Contact Mechanics. Cambridge University Press, Cambridge.

Keer, L.M., Parihar, K.S., 1978. Elastic stress singularities at conical inclusions. International Journal of Solids and Structures 14, 261–263.

Kikuchi, N., Oden, J.T., 1988. Contact Problem in Elasticity: A Study of Variational Inequalities and Finite Element Methods. SIAM, Philadelphia.

Krouskop, T.A., Wheler, T.M., Kaller, F., Garra, B.S., Hall, T., 1998. Elastic moduli of breast and prostate tissues under compression. Ultrasonic Imaging 20, 260–274.

Lee, M.R., Warne, D.P., Warne, P.G., 2004. On an incompressible nonlinearly elastic half-space under a compressive point load. Mathematics and Mechanics of Solids 19, 97–117.

Lim, Y.Y., Chaudhri, M.M., 2004. Indentation of elastic solids with rigid cones. Philosophical Magazine 84, 2877–2903.

Lysaght, V.E., DeBellis, A., 1969. Hardness Testing Handbook. American Chain and Cable Co., Bridgeport, CT.

Mooney, M., 1940. A theory of large elastic deformation. Journal of Applied Physics 11, 582–592.

Murnaghan, F.D., 1951. Finite Deformations of an Elastic Solid. Wiley, New York.

Ogden, R.W., 1984. Non-Linear Elastic Deformations. Eds. Harwood Series Mathematics and its Applications.

Person, B.N.J., 2000. Sliding Friction, Physical Principles and Applications, second ed. Springer, Berlin.

Picu, C.R., 1996. Stress singularities at vertices of conical inclusions with freely sliding interfaces. International Journal of Solids and Structures 33, 2453–2457.

Rivlin, R.S., 1953. The solution of the problem in second order elasticity theory. Journal of Rational Mechanics and Analysis 2, 53–81.

Sabey, B.E., 1958. Pressure distribution beneath spherical and conical shapes pressed into a rubber plane and their bearing on coefficient of friction under wet conditions. Proceedings of the Physical Society 71, 979–988.

Sabin, G.C., Kaloni, P.N., 1983. Contact problem of a rigid indentor in second order elasticity theory. Journal of Applied Mathematics and Physics 34, 370–386.

Schallamach, A., 1971. How does rubber slide? Wear 17, 30–312.

Selvadurai, AP.S., Spencer, A.J.M., 1972. Second-order elasticity with axial symmetry – I General theory. International Journal of Engineering Science 10, 97–114.

Shield, R.T., 1967. Inverse deformation results in finite elasticity. Journal of Applied Mathematics and Physics (ZAMP) 18, 490–500.

Simo, J.C., Taylor, R.L., Pister, K.S., 1985. Variational and projection methods for the volume constraint in finite deformation elasto-plasticity. Computer Methods in Applied Mechanics and Engineering 51, 177–208.

Simmonds, J.G., Warne, P.G., 1994. Notes on the nonlinearly elastic Boussinesq problem. Journal of Elasticity 34, 69–82.

Sneddon, I.N., 1972. The Use of Integral Transforms. Mc Graw-Hill, New York.

Soden, A.L., 1951. A Practical Manual of Rubber Hardness Testing. Maclaren and Sons, London.
Treloar, L.R.G., 1975. The Physics of Rubber Elasticity, 3rd ed. Clarendon Press, Oxford.
Vallet, D., Barquins, M., 2002. Adhesive contact and kinetics of adherence of a rigid conical punch on an elastic half-space (natural rubber). International Journal of Adhesion and Adhesives 22, 41–46.
Waggner, M.H., 1994. The origin of the C_2 term in rubber elasticity. Journal of Rheology 38, 655–679.
Wriggers, P., 2006. Computational Contact Mechanics, second ed. Springer, Netherlands.
Zheng, Y.P., Choi, Y.K., Wong, K., Chan, S., Mak, A.F., 2000. Biomechanical assessment of plantar foot tissue in diabetic patients using an ultrasound indentation system. Ultrasound in Medicine and Biology 2, 451–456.